Ionics (2017) 23:597–605
DOI 10.1007/s11581-016-1851-6

ORIGINAL PAPER

Pr-modified $Li_4Ti_5O_{12}$ nanofibers as an anode material for lithium-ion batteries with outstanding cycling performance and rate performance

Yuguang Zhao[1] · **Jianling Li**[1] · **Zhanyu Li**[1] · **Kai Yang**[2] · **Fei Gao**[2]

Received: 9 August 2016 / Revised: 20 September 2016 / Accepted: 29 September 2016 / Published online: 12 October 2016

Abstract Pr-doped $Li_4Ti_5O_{12}$ in the form of $Li_{4-x/3}Ti_{5-2x/3}Pr_xO_{12}$ (x = 0, 0.01, 0.03, 0.05, and 0.07) was synthesized successfully by an electrospinning technique. ICP shows that the doped samples are closed to the targeted samples. XRD analysis demonstrates that traces of Pr^{3+} can enlarge the lattice parameter of $Li_4Ti_5O_{12}$ from 8.3403 to 8.3765 Å without changing the spinel structure. The increase of lattice parameter is beneficial to the intercalation and de-intercalation of lithium-ion. XPS results identify the existence form of Ti is mainly Ti^{4+} and Ti^{3+} in minor quantity in $Li_{4-x/3}Ti_{5-2x/3}Pr_xO_{12}$ (x = 0.05) samples due to the small amount of Pr^{3+}. The transition from Ti^{4+} to Ti^{3+} is conducive to the electronic conductivity of $Li_4Ti_5O_{12}$. FESEM images show that all the nanofibers are well crystallized with a diameter of about 200 nm and distributed uniformly. The results of electrochemical measurement reveal that the 1D $Li_{4-x/3}Ti_{5-2x/3}Pr_xO_{12}$ (x = 0.05) nanofibers display enhanced high-rate capability and cycling stability compared with that of undoped nanofibers. The high-rate discharge capacity of the $Li_{4-x/3}Ti_{5-2x/3}Pr_xO_{12}$ (x = 0.05) samples is excellent (101.6 mAh g^{-1} at 50 °C), which is about 58.48 % of the discharge capacity at 0.2 °C and 4.3 times than that of the bare $Li_4Ti_5O_{12}$ (23.5 mA g^{-1}). Even at 10 °C (1750 mA g^{-1}), the specific discharge capacity is still 112.8 mAh g^{-1} after 1000 cycles (87.9 % of the initial discharge capacity). The results of cyclic voltammograms (CV) and electrochemical impedance spectroscopy (EIS) illustrate that the Pr-doped $Li_4Ti_5O_{12}$ electrodes possess better dynamic performance than the pure $Li_4Ti_5O_{12}$, further confirming the excellent electrochemical properties above.

Keywords Spinel $Li_4Ti_5O_{12}$ (LTO) · Anode material · Pr doping · Electrospinning · Lithium-ion battery

Introduction

Owing to recent requirements for electrical energy storage devices, increasing attention has been paid to spinal lithium-ion batteries (LIBs) with high power density and long cycle life [1, 2]. Currently, graphite, as a commercialized anode material, has been used as an active material of negative electrode (anode) for rechargeable lithium-ion batteries. However, it has a lot of problems in safety and life, which limits its practical applications seriously. Therefore, it is important to search for alternative anode materials with better safety and rate capability [3, 4].

Compared with graphite or other materials [5], spinel-type $Li_4Ti_5O_{12}$ shows some advantages in long life, low cost, and high security, which is largely due to the following three key characteristics. First, it has outstanding safety with a high insertion potential at around 1.55 V (vs. Li/Li^+), which can avoid the formation of SEI layers [6–9]. Second, its zero-strain structure makes it a promising material with a long cycle life during lithium-ion intercalation and de-intercalation [10]. Last but not the least, the rich content of Ti sources makes it a relatively cost-effective material [11]. However, $Li_4Ti_5O_{12}$ has a low electrical conductivity and Li ionic conductivity, resulting in poor full capacity at high charge-discharge rates and an initial capacity loss [12]. To improve the

✉ Yuguang Zhao
17801024767@163.com

✉ Jianling Li
lijianling@ustb.edu.cn

[1] School of Metallurgical and Ecological Engineering, University of Science and Technology Beijing, No.30 College Road, Beijing 100083, China

[2] China Electric Power Research Institute, Beijing 100085, China

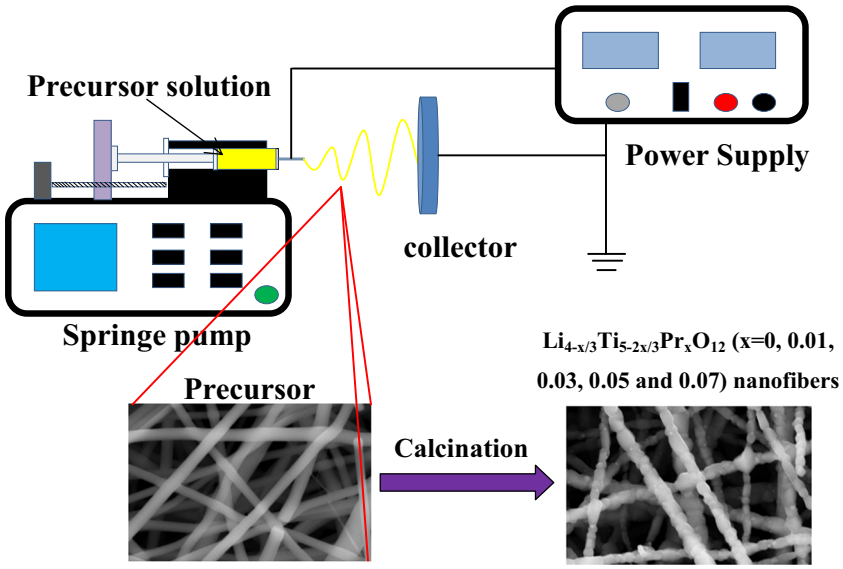

Scheme 1 Brief synthesis route of $Li_{4-x/3}Ti_{5-2x/3}Pr_xO_{12}$ (x = 0, 0.01, 0.03, 0.05, and 0.07) nanofibers

electrochemical properties in high current density, tremendous efforts have been made to enhance the electrical and ionic conductivity of $Li_4Ti_5O_{12}$. The most efficient methods are morphology altering [13, 14], surface coating [15–17], and element doping [18–20]. Surface coating can improve the electrical conductivity between $Li_4Ti_5O_{12}$ particles without enhancing the intrinsic electronic and Li ionic conductivities. Morphology altering and element doping can enhance them fundamentally. 1D nanostructures are beneficial to the electrochemical properties because the morphology can shorten Li^+ diffusion pathways and improve electron transport in lithium batteries [21]. What is more, the 1D nanostructures show advantages in uniformity and mass production compared with other methods, such as solid-state reaction, sol-gel method, or hydrothermal [22]. Large particle size element doping can also improve the electrochemical properties, such as La^{3+} [23], Ru^{4+} [24], and Sm^{3+} [25].

In this paper, we used rare earth element Pr^{3+} as the doping element (never been mentioned) and $Li_{4-x/3}Ti_{5-2x/3}Pr_xO_{12}$ (x = 0, 0.01, 0.03, 0.05, and 0.07) compounds were synthesized through electrospinning method. The electrochemical performance and structure were systematically investigated, and we found such composites with Pr doping are advantageous for enhancing the electronic conductivity and Li ionic conductivity, resulting in excellent rate capability and cycling stability.

Experimental

Sample preparation

$Li_{4-x/3}Ti_{5-2/3x}Pr_xO_{12}$ (x = 0, 0.01, 0.03, 0.05, and 0.07) compounds were synthesized by an electrospinning technique. Scheme 1 illustrates the brief synthesis route of the nanofibers. To get the bare $Li_4Ti_5O_{12}$, 0.03 mol of titanium (IV) isopropoxide and 0.0247 mol of lithium acetate were blended with 10 ml of ethanol and 21 ml of acetic acid. After magnetic stirring for 30 min, 0.9 g of polyvinylpyrrolidone (PVP) was added. Then the mixture was stirred for 1 h to obtain the precursor solution. To get the Pr-doped $Li_4Ti_5O_{12}$, different contents of praseodymium (III) nitrate with the ratio of $Li_{4-x/3}Ti_{5-2/3x}Pr_xO_{12}$ (x = 0, 0.01, 0.03, 0.05, and 0.07) were added to the precursor solution. The buff transparent solution was immediately put into a plastic syringe which linked to a high-voltage power supply. In order to increase the electrospinning production, the feeding rate for the precursor was set to 2.5 ml h^{-1}, which is five times than that of the average rate [26]. The distance between the tip of the needle and collector was 13 cm, and the voltage of the high-voltage power supply was 20 kV. After electrospinning, the nanowires were taken off from the collector. Ultimately, the nanofibers were calcined at 600 °C for 2 h and 750 °C for 5 h with a slow heating rate of 2 °C min^{-1} in air.

Table 1 Electrode materials $Li_{4-x/3}Ti_{5-2x/3}Pr_xO_{12}$ (x = 0, 0.01, 0.03, 0.05, and 0.07) synthesized in this work, based on ICP analysis

Samples	Theoretical molar content of Li:Ti:Pr	Experimental molar content of Li:Ti:Pr
x = 0	4:5:0	4.013:4.991:0
x = 0.01	3.997:4.993:0.01	4.009:4.987: 0.011
x = 0.03	3.990:4.980:0.03	3.992:4.981: 0.029
x = 0.05	3.983:4.967:0.05	3.988:4.959: 0.052
x = 0.07	3.977:4.953:0.07	3.989:4.956: 0.066

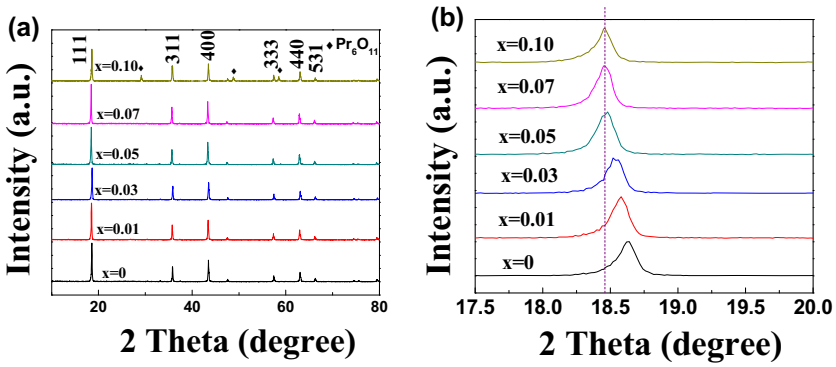

Fig. 1 **a** XRD patterns of synthesized $Li_{4-x/3}Ti_{5-2x/3}Pr_xO_{12}$ (x = 0, 0.01, 0.03, 0.05, 0.07, and 0.10) and **b** enlarged (111) peaks of samples with different doping amount of Pr

Material characterization

The relative contents of Li, Ti, and Pr in the prepared samples were monitored by inductively coupled plasma-atomic emission spectrometry (ICP, Perkin Optima 7000DV) analysis. The phase analysis of the prepared powders were performed by powder X-ray diffraction (XRD, Rigaku RINT2400, Japan) with Cu Kα radiation in 2θ degree ranging from 10 to 80° at a scanning rate of 10°/minute. The morphology and microstructure of the prepared powders were observed by field emission scanning electron microscopy (FESEM, Zeiss SuprATM 55, Germany) equipped with energy dispersive X-ray spectroscopy (EDS). The Brunauer–Emmett–Teller (BET, ASAP2010) model was adopted to calculate specific surface area and the density functional theory (DFT) method to determine pore-size distribution from the adsorption-desorption data. The surface chemistry composition and valence variation of all samples were investigated by X-ray photoelectron spectroscopy (XPS, Shimadzu Kratos Axis Ultra DLD) with Al K α radiation (1486.7 eV).

Electrode preparation

CR2025 coin cells were assembled to research the electrochemical performance of the work electrodes by galvanostatic charge-discharge test. The slurry was formed with 75 wt% as-prepared samples, 15 wt% acetylene black, and 10 wt% polyvinylidene fluoride (PVDF, as a binder), then, it was coated on the aluminum foil to form the work electrodes. After coating, the electrode was dried at 100 °C in vacuum oven for 12 h. 1.0 mol L^{-1} $LiPF_6$ was dissolved in a mixture—consist of 50 % ethylene carbonate (EC) and 50 % dimethyl carbonate (DMC)—as the electrolyte. The coin cells were assembled in an argon-filled glove box ($[O_2]$ <1 ppm, $[H_2O]$ <1 ppm) using the prepared electrode as cathode, pure lithium foil as anode and a Celgard 2400 as the separator.

Electrochemical characterization

The galvanostatic charge-discharge tests were carried out using a Land battery test system (LANHE CT2001A) between a cut-off voltage of 1 and 2.5 V. The rate capabilities of the as-prepared samples were measured at different rates of 0.2 °C (35 mA g^{-1}), 1 °C (175 mA g^{-1}), 5 °C (875 mA g^{-1}), 10 °C (1750 mA g^{-1}), 20 °C (3500 mA g^{-1}), 30 °C (5250 mA g^{-1}), 40 °C (7000 mA g^{-1}), and 50 °C (8750 mA g^{-1}). The cycling tests were conducted at 10 °C. The cyclic voltammetry (CV) curves were measured on a VMP2 electrochemical workstation under a scanning rate of 0.5 mV s^{-1} between 1.0 and 2.5 V (vs. Li/Li^+). Electrochemical impedance spectroscopy (EIS, Princeton Applied Research VersaSTAT3) at open-circuit voltage was performed with an AC voltage of 10 mV between 100 kHz and 10 MHz.

Results and discussions

According to inductively coupled plasma-atomic emission spectrometry (ICP), the doped samples were closed to the targeted samples, as shown in Table 1.

The XRD patterns of $Li_{4-x/3}Ti_{5-2x/3}Pr_xO_{12}$ (x = 0, 0.01, 0.03, 0.05, 0.07, and 0.10) samples are displayed in Fig. 1a. The major diffraction peaks of all annealed samples are in alignment to the standard diffraction pattern of $Li_4Ti_5O_{12}$ (JCPDS No. 49-–0207), which indicates that a small amount of Pr^{3+} doping does not change the cubic spinel structure of

Table 2 Lattice parameters of $Li_{4-x/3}Ti_{5-2x/3}Pr_xO_{12}$ (x = 0, 0.01, 0.03, 0.05 0.07, and 0.10)

Sample	x = 0	x = 0.01	x = 0.03	x = 0.05	x = 0.07	x = 0.10
Lattice parameter (Å)	8.3403	8.3483	8.3548	8.3765	8.3809	8.3817

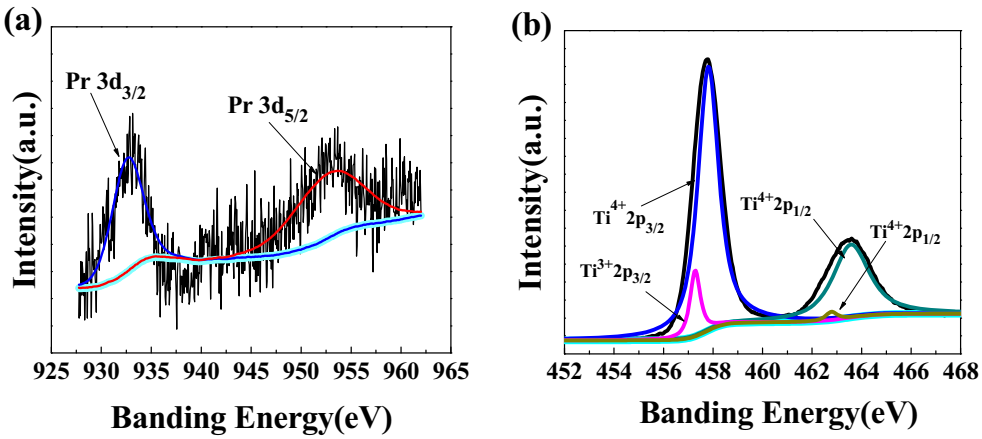

Fig. 2 **a** High-resolution XPS spectrum of Pr 3d in Pr-doped $Li_4Ti_5O_{12}$ (x = 0.05) and **b** Ti 2p in Pr-doped $Li_4Ti_5O_{12}$ (x = 0.05)

$Li_4Ti_5O_{12}$ with the space group of Fd3 m. No impurity peak can be detected in all samples, indicating that a small quantity of the dopant Pr^{3+} ions have successfully entered the lattice structure of $Li_4Ti_5O_{12}$ without causing any changes in

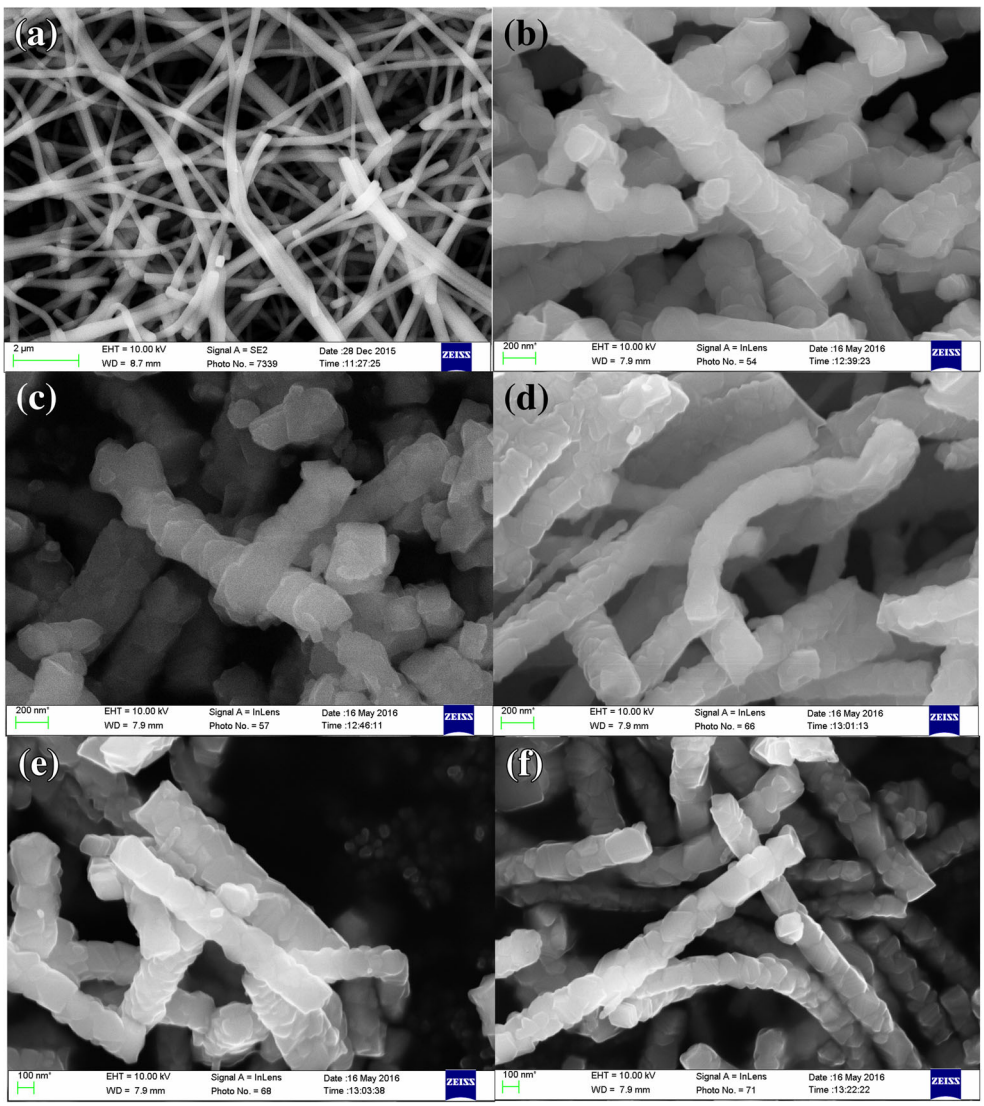

Fig. 3 SEM images of PVP/inorganic composite nanofibers after electrospinning (**a**); the bare $Li_4Ti_5O_{12}$ (**b**) and the $Li_{4-x/3}Ti_{5-2x/3}Pr_xO_{12}$ (x = 0.01, 0.03, 0.05 and 0.07) samples as follows: x = 0.01 (**c**), x = 0.03 (**d**), x = 0.05 (**e**), and x = 0.07 (**f**) after calcination and grinding

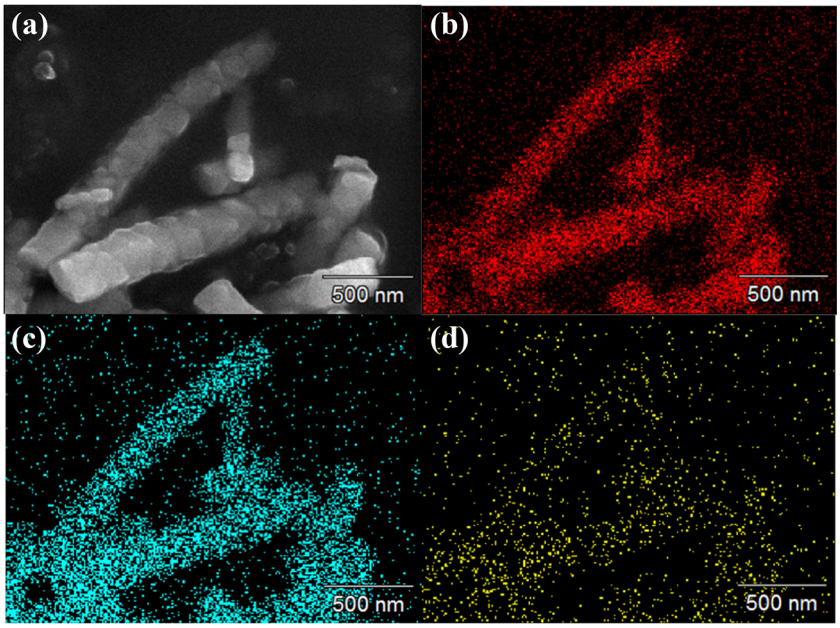

Fig. 4 FESEM image of $Li_{4-x/3}Ti_{5-2x/3}Pr_xO_{12}$ (x = 0.05) (**a**), and the corresponding EDS element mapping of O (**b**), Ti (**c**), and Pr (**d**) of the $Li_{4-x/3}Ti_{5-2x/3}Pr_xO_{12}$ (x = 0.05) particles

structural characteristics. However, some impurities are detectable when x = 0.10, denoting that the excess Pr cannot be doped into the LTO and it exists in the form of Pr_6O_{11}. In order to certify that the lattice distortion of Pr-doped $Li_4Ti_5O_{12}$ has taken place, the peak positions of (111) planes of all samples are enlarged and shown in Fig. 1b. It is easy to find a slight structural change of the XRD patterns between pristine $Li_4Ti_5O_{12}$ and Pr-doped $Li_4Ti_5O_{12}$ in close inspection. Compared with that of the pristine $Li_4Ti_5O_{12}$, the (111) peaks of the $Li_{4-x/3}Ti_{5-2x/3}Pr_xO_{12}$ (x = 0.01, 0.03, 0.05, 0.07, and 0.10) shift to smaller angles after Pr doping, revealing that the lattice parameter increases gradually with increasing Pr doping amount. What is more, $Li_{4-x/3}Ti_{5-2x/3}Pr_xO_{12}$ (x = 0.05, 0.07, and 0.10) shows similar (111) peaks, indicating that when x = 0.07, a small amount of Pr is excess, which hinders the improvement of electrochemical properties. The lattice parameters are calculated and the data obtained from XRD are listed in Table 2. The results show that the lattice parameter increases as the increase of the doping amount of Pr $(NO)_3$. The reasons for the changes of lattice parameter after Pr modifying in all samples may be the following fact: Pr^{3+} ion (0.113 nm [27]) has a lager ionic radius than Li^+ (0.076 nm [28]) and Ti^{4+} (0.0605 nm [28]) in the octahedral 16d sites and in the structure, and every two Ti^{4+} and one Li^+ may be replaced with three Pr^{3+} [29]. Ultimately, the lattice parameter is slightly enlarged, which is beneficial for lithium batteries in lithium-ion intercalation and de-intercalation. It indicates that the fast Li^+ diffusion caused by Pr doping will improve the electrochemical performance.

X-ray photoelectron spectroscopy (XPS) was carried out to prove the existence of Pr and confirm the valence variation of Ti in $Li_{4-x/3}Ti_{5-2x/3}Pr_xO_{12}$ (x = 0.05). Figure 2a shows the XPS spectrum of Pr 3d. The XPS spectrum of Pr 3d exhibits two characteristic binding energy peaks of 933.5 and 954 eV, corresponding to Pr $3d_{3/2}$ and Pr $3d_{5/2}$ [30], indicating that Pr^{3+} has embedded into the $Li_4Ti_5O_{12}$ lattice and no Pr_2O_3

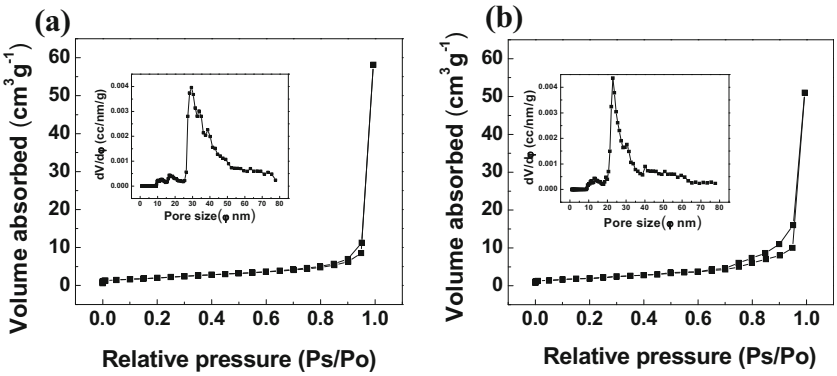

Fig. 5 Nitrogen adsorption-desorption isotherms of $Li_{4-x/3}Ti_{5-2x/3}Pr_xO_{12}$ for x = 0 (**a**) and 0.05 (**b**). The *insets* are the corresponding DFT pore-size distribution curves

phase appears. The high-resolution XPS spectrum of Ti 2p in $Li_{4-x/3}Ti_{5-2x/3}Pr_xO_{12}$ (x = 0.05) is shown in Fig. 2b. In Fig. 2b , two pairs of peaks can be found. One pair at 458.2 and 464.2 eV stands for Ti $2p_{3/2}$ and Ti $2p_{1/2}$ of Ti^{4+} and the other pair at 457.1 and 462.4 eV stands for Ti $2p_{3/2}$ and Ti $2p_{1/2}$ of Ti^{3+}. It is vigorously confirmed that some oxygen vacancies have generated in order to maintain the charge balance from Ti^{4+} to Ti^{3+} due to Pr doping. The valence state change of Ti ion from Ti^{4+} to Ti^{3+} or the oxygen vacancies are conducive to electrochemical properties, which has been mentioned many times [31, 32].

To meet the requirements of 1D morphology and excellent electrical conductivity, the smooth PVP/inorganic composite nanofibers were synthesized through electrospinning method and the morphology was characterized by SEM, as shown in Fig. 3a. After calcination and grinding, the morphologies of the as-prepared $Li_{4-x/3}Ti_{5-2x/3}Pr_xO_{12}$ (x = 0, 0.01, 0.03, 0.05, and 0.07) samples are shown in Fig. 3b–f. It is not hard to find that the images of the Pr-doped and undoped $Li_4Ti_5O_{12}$ powders are similar, and they are all composed of nanorods with a uniform size distribution. The diameters of the nanofibers are about 0.2 μm. Figure 4a shows the FESEM image of $Li_{4-x/3}Ti_{5-2x/3}Pr_xO_{12}$ (x = 0.05) and the rest of Fig. 4 are the corresponding EDS element mapping of O (Fig. 4b), Ti (Fig. 4c), and Pr (Fig. 4d) of $Li_{4-x/3}Ti_{5-2x/3}Pr_xO_{12}$ (x = 0.05) particles. It is obvious to find that the shape of the FESEM image and the EDS element mapping images are similar, which indicates that the Pr element distributes uniformly in Pr-doped $Li_4Ti_5O_{12}$ (x = 0.05).

Figure 5 shows the N_2 adsorption-desorption isotherms and the DFT pore-size distribution curve (inset) of $Li_{4-x/3}Ti_{5-2x/3}Pr_xO_{12}$ (x = 0 and x = 0.05). The N_2 adsorption-desorption isotherms are identified as the type IV (IUPAC classification) [33]. From the pore-size distribution curves depicted in the insets, the pore size of the bare LTO is 29.4 nm and the surface area is 7.9 $m^2\ g^{-1}$ (Fig. 5a). The Pr doping also gives rise to uniformity of pore-size distribution. $Li_{4-x/3}Ti_{5-2x/3}Pr_xO_{12}$ (x = 0.05) has a pore size of 23.6 nm and a surface area of 10.6 $m^2\ g^{-1}$ (Fig. 5b). The nanoparticles with large surface area are conducive to accelerating the electrode reaction, shortening the diffusion path of Li ions, and facilitating charge transfer.

In order to certify the effect of Pr doping on improving the rate capability, different doping contents of $Li_4Ti_5O_{12}$ at different rates of 0.2, 1, 5, 10, 20, 30, 40, and 50 °C were tested, and the results are shown in Fig. 6. Each stage of the charge-discharge processes were tested for 3 cycles. It is obvious that the discharge capacity decreases as the discharge current rate increases from 0.2 to 50 °C. Meanwhile, it is not difficult to find that the discharge capacity of Pr-doped samples decreased less than that of undoped $Li_4Ti_5O_{12}$ samples when the discharge current increased, especially at a high rate. The button batteries assembled with undoped materials show a bad

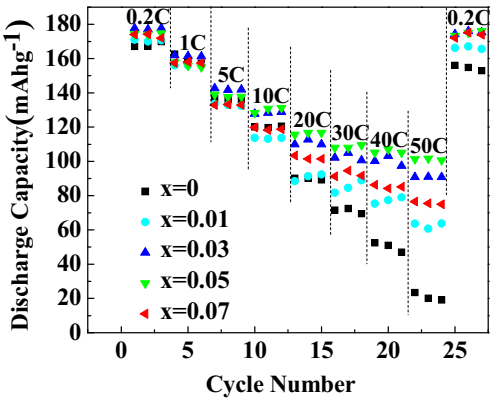

Fig. 6 Rate capabilities of $Li_{4-x/3}Ti_{5-2x/3}Pr_xO_{12}$ (x = 0, 0.01, 0.03, 0.05, and 0.07) samples at different cycling rates

performance with the discharge capacity of 23.5 mAh g^{-1}, which indicates that the insertion/de-insertion progress proceeds unsmoothly. However, when using the doping ratio of x = 0.05 materials, the discharge capacity is much better (101.6 mAh g^{-1}, 4.3 times of the undoped samples and 58 % of the theoretical specific capacity). Table 3 shows the initial discharge capacity at different rates of $Li_{4-x/3}Ti_{5-2x/3}Pr_xO_{12}$ (x = 0 and 0.05).

In order to compare the insertion/de-insertion progress between the bare $Li_4Ti_5O_{12}$ and $Li_{4-x/3}Ti_{5-2x/3}Pr_xO_{12}$ (x = 0.05), the initial charge-discharge curves of them are shown in Fig. 7. The cycling rates are from 0.2 to 50 °C and the potential window is between 1.0 and 2.5 V. From the figure, it is easy to observe that the charge-discharge curves have distinct potential plateaus around 1.5 V (vs. Li/Li^+) at 0.2 and 1 °C for both of the two electrodes, which is consistent with the two-phase insertion reaction between $Li_4Ti_5O_{12}$ and $Li_7Ti_5O_{12}$. With the increase of the charge-discharge current density for both of the two samples, the charge plateau increases and discharge plateau decreases, indicating that the overpotential between the electrode and the electrolyte increases. Compared with the Pr-doped samples, the discharge plateaus can be hardly found in pure $Li_4Ti_5O_{12}$ samples at 50 °C. The high polarization resistance of the pure samples is the main reason for this phenomenon [34]. The $Li_{4-x/3}Ti_{5-2x/3}Pr_xO_{12}$ (x = 0.05) shows an obvious discharge plateau at 30, 40, and 50 °C, and there is only a small reduction from 30 to 50 °C, demonstrating that the polarization resistance decreases due to the doping element of Pr. Nevertheless, among all of the Pr-doped

Table 3 Reversible capacities (mAh g^{-1}) of $Li_{4-x/3}Ti_{5-2x/3}Pr_xO_{12}$ (x = 0 and 0.05) at various current rates

	Current rates (°C)			
x in $Li_{4-x/3}Ti_{5-2x/3}Pr_xO_{12}$	0.2	5	20	50
0	167.3	136.6	90.1	23.5
0.05	173.8	139	115.7	101.6

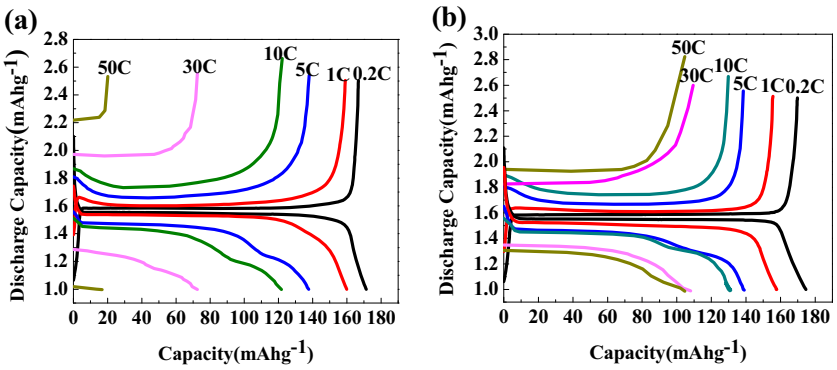

Fig. 7 The initial charge-discharge curves of bare $Li_4Ti_5O_{12}$ (**a**) and $Li_{4-x/3}Ti_{5-2x/3}Pr_xO_{12}$ (x = 0.05) (**b**)

samples, the $Li_{4-x/3}Ti_{5-2x/3}Pr_xO_{12}$ (x = 0.05) shows the best performance in rate capability. The main reason may be the fact that excess dopant of Pr^{3+}, in Li^+, and Ti^{4+} sites will gradually increase the transfer resistance (R_{ct}).

Cyclic performance of $Li_{4-x/3}Ti_{5-2x/3}Pr_xO_{12}$ (x = 0, 0.01, 0.03, 0.05, and 0.07) at 10 °C rate is shown in Fig. 8. Compared with the bare $Li_4Ti_5O_{12}$, Pr-doped $Li_4Ti_5O_{12}$ batteries exhibit higher reversible capacities. Among all the Pr-doped electrodes, the initial discharge capacity of $Li_{4-x/3}Ti_{5-2x/3}Pr_xO_{12}$ (x = 0.05) is 128.3 and 112.8 mAh g^{-1} through 1000 cycles at 10 °C. The capacity retention rate is 87.9 %. However, the bare $Li_4Ti_5O_{12}$ has a relatively inferior discharge capacity from 105.9 to 53 mAh g^{-1}. The capacity retention rate is only 50.05 %. The reason why a small amount of Pr is beneficial to the cycling performance is that the lattice constant is enlarged due to the doping of Pr, which makes it easier for the insertion and extraction of Li^+ ions and enhances the stability of the structure. The result is consistent with the rate capabilities. Hence, the Pr-doped $Li_4Ti_5O_{12}$ is considered to be an excellent electrode material, especially when x = 0.05.

Cyclic voltammograms (CV curves) of $Li_{4-1/3x}Ti_{5-2/3x}Pr_xO_{12}$ (x = 0, 0.01, 0.03, 0.05, and 0.07) samples as active materials at a scanning rate of 0.5 mV s^{-1} between 1.0 and 2.5 V are shown in Fig. 9. They have similar appearance with only a pair of reversible redox peaks, suggesting that the electrochemical reaction processes of them are similar and the redox reaction of $Li_4Ti_5O_{12}$ was not affected by Pr doping. The cathodic peak is located at about 1.45 V (vs. Li/Li^+), corresponding to the voltage plateau of the first discharge process of Li^+ intercalated into $Li_4Ti_5O_{12}$ anode [35]. There is also an anodic peak at about 1.75 V (vs. Li/Li^+), which corresponds to the voltage plateau of the first charge process of Li^+ de-intercalated from the anode [35]. The differences between anodic peaks and cathodic peaks are given in Table 4. The potential differences of Pr-doped $Li_4Ti_5O_{12}$ sample are smaller than those of undoped $Li_4Ti_5O_{12}$, indicating that Pr doping has improved the electrochemical properties. From Table 4, we can also find the anodic peak and cathodic peak of $Li_{4-1/3x}Ti_{5-2/3x}Pr_xO_{12}$ (x = 0.05) are located at 1.697 and 1.491 V. The difference between them is 206 mV, which is the smallest in all samples. The cyclic voltammograms are in accordance with the results of the tests, further illustrating that the Pr-doped $Li_4Ti_5O_{12}$ electrodes possess better kinetics than the pure $Li_4Ti_5O_{12}$.

To compare the differences in electrochemical properties between $Li_{4-x/3}Ti_{5-2x/3}Pr_xO_{12}$ (x = 0, 0.01, 0.03, 0.05, and 0.07) electrodes, the electrochemical impedance spectroscopy (EIS) measurement is conducted at open-circuit voltages after 300 cycles of charge and discharge at 10 °C. The corresponding Nyquist plots are displayed in Fig. 10 and they are

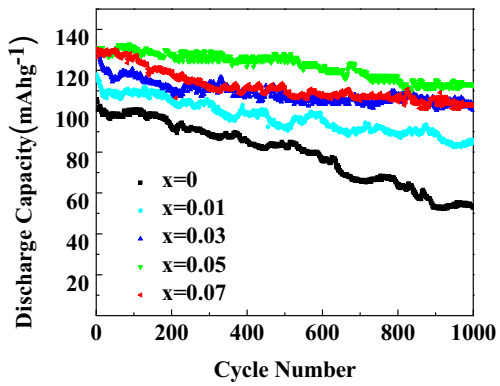

Fig. 8 Cyclic performance of $Li_{4-x/3}Ti_{5-2x/3}Pr_xO_{12}$ (x = 0, 0.01, 0.03, 0.05, and 0.07) at 10 °C rate

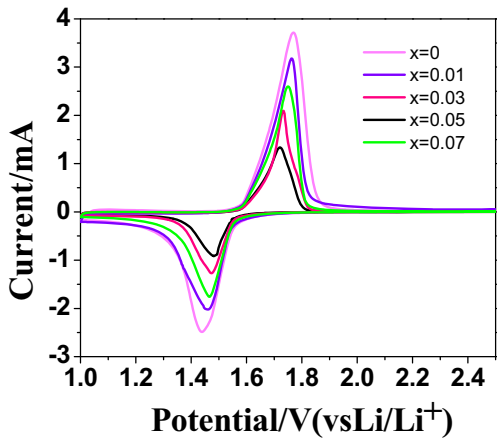

Fig. 9 CV curves of $Li_{4-x/3}Ti_{5-2x/3}Pr_xO_{12}$ (x = 0, 0.01, 0.03, 0.05, and 0.07) with a scanning rate of 0.5 mV s^{-1}

Table 4 Potential differences between anodic and cathodic peaks of $Li_{4-x/3}Ti_{5-2x/3}Pr_xO_{12}$ (x = 0, 0.01, 0.03, 0.05, and 0.07) electrodes for the fresh cells

Sample	φ_a/V	φ_c/V	$(\varphi_a-\varphi_c)mV$
(x = 0)	1.734	1.431	0.303
(x = 0.01)	1.727	1.462	0.265
(x = 0.03)	1.702	1.475	0.227
(x = 0.05)	1.697	1.491	0.206
(x = 0.07)	1.721	1.469	0.252

composed of one semicircle at high frequency and a sloping straight line at low frequency. The diameter of the semicircle stands for the meaning of charge transfer resistance (R_{ct}) and the sloping straight line is related to the Warburg impedance [36]. From Fig. 9a, it is easy to find that the diameter of the semicircle of Pr-doped $Li_4Ti_5O_{12}$ is shorter than that of bare $Li_4Ti_5O_{12}$, suggesting that a small amount of Pr doping is beneficial to the electronic conductivity of $Li_4Ti_5O_{12}$. The experimental result is fitted using an equivalent circuit in the inset of Fig. 10. In the inset, R_s is the ohmic resistance of electrolyte, R_{ct} is the charge transfer resistance, W is the Warburg impedance of solid-phase diffusion, and CPE is the constant phase element [37]. The results of the EIS for $Li_{4-x/3}Ti_{5-2x/3}Pr_xO_{12}$ (x = 0, 0.01, 0.03, 0.05, and 0.07) are shown in Table 5, indicating that a small amount of Pr^{3+} doping can result in a higher lithium-ion diffusion coefficient and a lower electrode polarization.

Conclusions

In this paper, well-structured cubic spinel $Li_{4-x/3}Ti_{5-2x/3}Pr_xO_{12}$ (x = 0, 0.01, 0.03, 0.05, and 0.07) nanofibers were successfully synthesized through electrospinning method. ICP

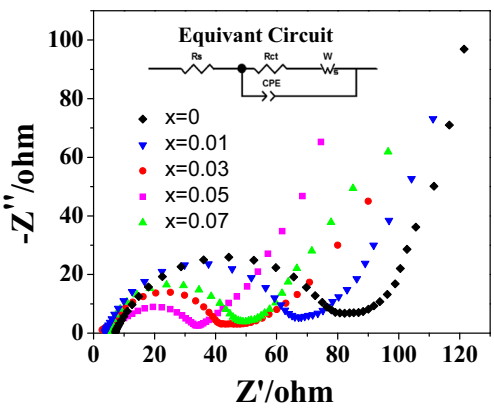

Fig. 10 Nyquist plots of $Li_{4-x/3}Ti_{5-2x/3}Pr_xO_{12}$ (x = 0, 0.01, 0.03, 0.05, and 0.07) samples at the voltage of 1.55 V (vs. Li/Li^+) from 100 kHz to 10 MHz

Table 5 Results of the EIS for $Li_{4-x/3}Ti_{5-2x/3}Pr_xO_{12}$ (x = 0, 0.01, 0.03, 0.05, and 0.07)

Sample	R_s/Ω	R_{ct}/Ω
x = 0	2.147	94.1
x = 0.01	1.78	68.26
x = 0.03	1.34	43.58
x = 0.05	2.13	53.98
x = 0.07	2.45	58.41

shows that the doped samples are close to the targeted samples and a small amount of Pr doping does not change the bulk structure of $Li_4Ti_5O_{12}$. Among all the Pr-doped samples, $Li_{4-x/3}Ti_{5-2x/3}Pr_xO_{12}$ (x = 0.05) exhibits the best properties in high-rate capability and cyclic performance. The high-rate discharge capacity of the $Li_{4-x/3}Ti_{5-2x/3}Pr_xO_{12}$ (x = 0.05) sample is excellent (101.6 mAh g^{-1} at 50 °C), which is about 58.48 % of the discharge capacity at 0.2 °C and 4.3 times than that of the bare $Li_4Ti_5O_{12}$. Even at 10 °C (1750 mA g^{-1}), the specific discharge capacity is still 112.8 mAh g^{-1} after 1000 cycles. Compared with the bare $Li_4Ti_5O_{12}$, the $Li_{4-x/3}Ti_{5-2x/3}Pr_xO_{12}$ (x = 0.05) shows smaller electrochemical impedance and electrochemical polarization at high-rate charge-discharge processes. All the results suggest that the outstanding electrochemical properties benefit from Pr doping and the $Li_{4-x/3}Ti_{5-2x/3}Pr_xO_{12}$ (x = 0.05) nanofibers make it a promising anode material for lithium-ion battery.

Acknowledgments The work was supported by the Science and Technology Project of State Grid Corporation of China (DG71-15-042) and the National Natural Science Foundation of China (nos. 51572024 and 51172023).

References

1. Armand M, Tarascon J-M (2008) Building better batteries. Nature 451:652–657
2. Yuan T, Cai R, Gu P, Shao Z (2010) Synthesis of lithium insertion material $Li_4Ti_5O_{12}$ from rutile TiO_2 via surface activation. J Power Sources 195:2883–2887
3. Zhu W, Huang H, Gan Y et al (2014) Mesoporous cobalt monoxide nanorods grown on reduced graphene oxide nanosheets with high lithium storage performance. Electrochim Acta 138:376–382
4. Yi T-F, Yang S-Y, Xie Y (2015) Recent advances of $Li_4Ti_5O_{12}$ as a promising next generation anode material for high power lithium-ion batteries. J Mater Chem A 3:5750–5777
5. Wen W, Wu J, Jiang Y et al (2015) Anatase TiO_2 ultrathin nanobelts derived from room-temperature-synthesized titanates for fast and safe lithium storage. Sci Rep 5:11804
6. Lu X, Zhao L, He X et al (2012) Lithium storage in $Li_4Ti_5O_{12}$ spinel: the full static picture from electron microscopy. Adv Mater 24:3233–3238
7. Pan H, Zhao L, Hu YS et al (2012) Improved Li-storage performance of $Li_4Ti_5O_{12}$ coated with C–N compounds derived from pyrolysis of urea through a low-temperature approach. Chem Sus Chem 5:526–529
8. Pan H-L, Hu Y-S, Li H, Chen L-Q (2011) Significant effect of electron transfer between current collector and active material on

high rate performance of $Li_4Ti_5O_{12}$. Chinese Phys B 20:118202-1–118202-4
9. Jia Z, Zhou Q, Li X et al (2015) Effect of rigidity of porous structure on electrochemical behavior of pristine $Li_4Ti_5O_{12}$ microspheres. Electrochim Acta 156:216–222
10. Chang L, Luo S, Zhang H et al (2014) Synthesis and performance of $Li_4Ti_5O_{12}$ anode materials using the PVP-assisted combustion method. Chinese Chem Lett 25:1569–1572
11. Ohzuku T, Ueda A, Yamamoto N (1995) Zero-strain insertion material of Li $[Li_{1/3}Ti_{5/3}]O_4$ for rechargeable lithium cells. J Electrochem Soc 142:1431–1435
12. Ouyang CY, Zhong ZY, Lei MS (2007) Ab initio studies of structural and electronic properties of $Li_4Ti_5O_{12}$ spinel. Electrochem Commun 9:1107–1112
13. Ma Y, Ding B, Ji G, Lee JY (2013) Carbon-encapsulated F-doped $Li_4Ti_5O_{12}$ as a high rate anode material for Li^+ batteries. ACS Nano 7:10870–10878
14. Wang J, Shen L, Li H et al (2014) Mesoporous $Li_4Ti_5O_{12}$/carbon nanofibers for high-rate lithium-ion batteries. J Alloys Compd 587: 171–176
15. Peng J, Zuo Y-T, Li G, Wang G (2016) Preparation of few-layer reduced graphene oxide-wrapped mesoporous $Li_4Ti_5O_{12}$ spheres and its application as an anode material for lithium-ion batteries. Chinese Chem Lett:10–13
16. Shen L, Yuan C, Luo H et al (2011) In situ growth of $Li_4Ti_5O_{12}$ on multi-walled carbon nanotubes: novel coaxial nanocables for high rate lithium ion batteries. J Mater Chem 21:761–767
17. Liu G-QG-Y, Wang H-Y, Liu G-QG-Y et al (2013) Synthesis and electrochemical performance of high-rate dual-phase $Li_4Ti_5O_{12}$-TiO_2 nanocrystallines for Li-ion batteries. Electrochim Acta 87:218–223
18. Li F, Zeng M, Li J et al (2016) Sb doped $Li_4Ti_5O_{12}$ hollow spheres with enhanced lithium storage capability. RSC Adv 6:26902–26907
19. Bai Y-J, Gong C, Lun N, Qi Y-X (2013) Yttrium-modified $Li_4Ti_5O_{12}$ as an effective anode material for lithium ion batteries with outstanding long-term cyclability and rate capabilities. J Mater Chem A:89–96
20. Zhang Q, Liu Y, Lu H et al (2016) Ce^{3+}-doped $Li_4Ti_5O_{12}$ with CeO_2 surface modification by a sol-gel method for high-performance lithium-ion batteries. Electrochim Acta 189:147–157
21. Kim J, Shi D, Kong K et al (2013) Structurally and electronically designed TiO_2N_x. ACS Appl Mater Interfaces 5:691–696
22. Huang S, Wen Z, Zhu X, Gu Z (2004) Preparation and electrochemical performance of Ag doped $Li_4Ti_5O_{12}$. Electrochem Commun 6: 1093–1097
23. Yang S-Y, Yuan J, Zhu Y-R et al (2015) Structure and electrochemical properties of Sc^{3+}-doped $Li_4Ti_5O_{12}$ as anode materials for lithium-ion battery. Ceram Int 41:7073–7079
24. Jhan YR, Lin CY, Duh JG (2011) Preparation and characterization of ruthenium doped $Li_4Ti_5O_{12}$ anode material for the enhancement of rate capability and cyclic stability. Mater Lett 65:2502–2505
25. Li Z, Li J, Zhao Y et al (2016) Structure and electrochemical properties of Sm-doped $Li_4Ti_5O_{12}$ as anode material for lithium-ion batteries. RSC Adv 6:15492–15500
26. Jo MR, Jung YS, Kang Y-M (2012) Tailored $Li_4Ti_5O_{12}$ nanofibers with outstanding kinetics for lithium rechargeable batteries. Nanoscale 4:6870
27. Su W, Chen J, Wu L et al (2008) Visible light photocatalysis on praseodymium (III)-nitrate-modified TiO_2 prepared by an ultrasound method. Appl Catal B Environ 77:264–271
28. Yi T-F, Liu H, Zhu Y-R et al (2012) Improving the high rate performance of $Li_4Ti_5O_{12}$ through divalent zinc substitution. J Power Sources 215:258–265
29. Zhang Q, Verde MG, Seo JK et al (2015) Structural and electrochemical properties of Gd-doped $Li_4Ti_5O_{12}$ as anode material with improved rate capability for lithium-ion batteries. J Power Sources 280:355–362
30. Hsieh PT, Chen YC, Kao KS, Wang CM (2008) Luminescence mechanism of ZnO thin film investigated by XPS measurement. Appl Phys A Mater Sci Process 90:317–321
31. Qi Y, Huang Y, Jia D et al (2009) Preparation and characterization of novel spinel $Li_4Ti_5O_{12-x}Br_x$ anode materials. Electrochim Acta 54:4772–4776
32. Wolfenstine J, Allen JL (2008) Electrical conductivity and charge compensation in Ta doped $Li_4Ti_5O_{12}$. J Power Sources 180:582–585
33. Liu G-Y, Wang H-Y, Liu G-Q et al (2012) Facile synthesis of nanocrystalline Li4Ti5O12 by microemulsion and its application as anode material for Li-ion batteries. J Power Sources 220:84–88
34. Wang D, Zhang CM, Zhang YY, Wang J, He DN (2013) Synthesis and electrochemical properties of La-doped $Li_4Ti_5O_{12}$ as anode material for Li-ion battery. Ceram Int 39:5145–5149
35. Zhang Y, Zhang C, Lin Y et al (2014) Influence of Sc^{3+} doping in B-site on electrochemical performance of $Li_4Ti_5O_{12}$ anode materials for lithium-ion battery. J Power Sources 250:50–57
36. Zhu Yang H, Zhang W, Huang H, Tao X, Xia Y, Gan Y, Guo XW (2015) Synthesis and electrochemical performance of $Li_4Ti_5O_{12}$/TiO_2/C nanocrystallines for high-rate lithium ion batteries. RSC Adv 5:74774–74782
37. Shenouda AY, Murali KR (2008) Electrochemical properties of doped lithium titanate compounds and their performance in lithium rechargeable batteries. J Power Sources 176:332–339